Stopping of relativistic electrons in a partially degenerate electron fluid

K. V. Starikov* and C. Deutsch
LPGP (UMR-CNRS 8578), Bâtiment 210, Universite Paris-Sud, 91405 Orsay Cedex, France
(Received 1 June 2004; revised manuscript received 7 October 2004; published 22 February 2005)

The stopping mechanisms of relativistic electron beams in superdense and partially degenerate electron fluid targets are investigated in the framework of the fast ignitor concept for inertial confinement fusion. In order to comply with specific demands in this area, we focus attention on the target partial degeneracy parameter $\theta = T_e/T_f$, in terms of the thermal to Fermi temperature ratio. The target electron fluid is thus modeled very accurately with a random phase approximation dielectric function. The stopping results are shown to be very weakly θ dependent. However, a quantum target description is needed to recover their correct increasing trend with increasing projectile energy. The ranges and effective penetration depths in precompressed thermonuclear fuels are shown to be nearly a factor of 2 shorter than earlier classical estimates in the same conditions. The overall conclusions pertaining to the feasibility of fast ignition thus remain unchanged.

DOI: 10.1103/PhysRevE.71.026407 PACS number(s): 52.50.Gj, 52.40.Mj, 52.25.Mq, 52.57.Kk

I. INTRODUCTION

For several years, the interaction of very intense relativistic electron beams (REB's) with superdense and precompressed deuterium+tritium (DT) thermonuclear fuel has remained a field of rather intense scrutiny [1–3]. This trend is largely motivated by advanced and sophisticated proposals advocating a careful time sequencing of the target fuel compression followed by ignition. It is well known that the former process is a thousand times cheaper than the latter [4]. So it has been a continuous struggle in the field of inertial confinement fusion (ICF) to disentangle as much as possible the compression phase from the climax culminating in ignition.

Fusion physicists have presently convinced themselves that such a decoupling is now feasible with the use of the so-called petawatt (PW) lasers [5,6]. These lasers, operating on a very short timescale, of the order of a fraction of a picosecond, can produce very intense REB's, in the MeV energy range, when focused on a cold or hot plasma interface. This beneficial feature is largely, but not totally, due to ponderomotive acceleration.

These REB's have been demonstrated able to produce easily a well-localized hot plasma (hot spot) in the precompressed fuel. In this regard, it should be mentioned that the total decoupling of ignition from compression allows us to consider indifferently any driver: laser, heavy ion, Z pinch, etc. for the initial compression phase.

The figure of merit qualifying the success of this sequential ignition, also called fast ignition (FI), is the REB penetration distance in the densest part of the DT core, at 300 g/cm^3, which corresponds to an electron number density $n \sim 10^{26}$ cm^{-3}. The compressed core usually presents itself as a spherical pellet with a diameter $\sim 30-60$ μm. The outer layers are less dense with a continuous density gradient down to the core (Fig. 1).

REB's with 1 MeV kinetic energy should have a penetration depth ~ 10 μm which is also the nearly rectilinear stopping distance for the 3.5 MeV thermonuclear α particles required to sustain an exoenergetic fusion process. The latter is dynamically secured by having the produced hot spot travel through the remaining cold compressed fuel. Typically, heating initially and selectively 2% [4] of this cold fuel should prove sufficient for running a successful and economically rewarding fast ignition.

The envisioned fast ignition scheme driven by a PW-laser-produced REB is schematically outlined on Fig. 1. We expect the given hot spot plasma to be located somewhat off center, in contradistinction to the usual scheme based on central spot ignition, where ignition features the unavoidable conclusion of a sudden entropy rise in the overcompressed fuel.

As far as local heating of compressed DT plasma is considered, it should be recalled that most of the REB kinetic energy gets transferred to the target electron fluid (TEF) through relativistic stopping mechanisms detailed below. Subsequently, the TEF equilibrates its temperature with the target ion fluid (TIF) and heats it to thermonuclear temperature. Earlier and related investigations have been restricted to a classical TEF description.

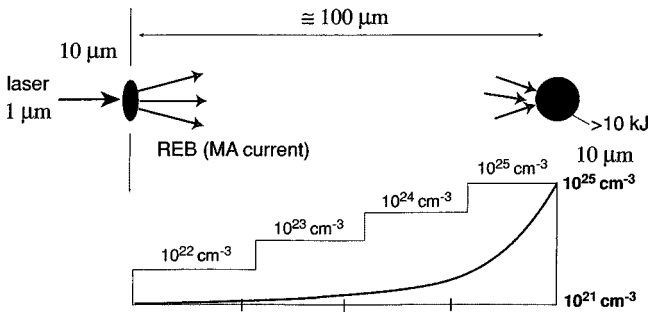

FIG. 1. Relativistic electron beam propagation with MeV incoming energy through layers of increasing density N_p in a core of precompressed DT fuel.

*Present address: Department of Physics, Kazakh National University, Tole Bi 96, ALMATY 480012, Kazakhstan.

 ©2005 The American Physical Society

The intense efforts, both experimental and numerical, presently developing in the field of beam-target interaction of FI concern have motivated us to revisit the conclusions of the classical approach. We thus pay attention to the TEF arbitrary degeneracy $\theta = T_e/T_f$ which is due to the very high density $n \geqslant 10^{23}$ e cm^{-3} as well as the thermal temperature T_e which can remain at a modest level in view of the envisioned adiabatic precompression [4]. According to standard FI scenarios [1,2] (see Fig. 1) T_f takes values between 8 eV at the outer surface and nearly 800 eV in the dense core. The classical description is thus equivalent to the high temperature limit. We thus intend to pinpoint any significant departure from this limit for the REB range and penetration depth in the TEF.

The present paper is structured as follows. In Sec. II, the random phase approximation (RPA) is seen to be fully adequate to qualify the θ-dependent TEF dielectric function $\varepsilon(k,\omega)$.

This formulation is then used in Sec. III to implement a Landau scheme for REB relativistic stopping in the given TEF. The density profile of the precompressed DT core is approximated by a steplike profile (Fig. 1) to allow us to restrict attention to a homogeneous target approximation.

The global features of relativistic stopping are detailed in Sec. IV. These include density dependence as well as variations of the REB kinetic energy. Ranges and penetration depths are considered in Sec. V, while multiple and elastic scattering of projectile electrons on the TIF are also taken into account. These results are finally contrasted with earlier classical ones in the outlook Sec. VI, where we also provide some estimates of e-foldings pertaining to the transverse electromagnetic Weibel instability in order to secure a dominant collisional regime for REB stopping in the precompressed plasma target.

II. PARTIALLY DEGENERATE ELECTRON FLUID

Temperature-dependent dielectric functions for dense TEF's have been extensively investigated, within a homogeneous approximation [7–10] initiated by Skupsky in the context of laser direct driven ICF [7]. At very high target densities, as in the present case, one expects the random phase approximation to provide an excellent model. Correcting it through local field correction (LFC) [11] factors $G_e(k)$, in Fourier space, one can thus secure a well-behaved large k (small distance) behavior through the standard formulation

$$\varepsilon(k,\omega) = 1 - \frac{\varphi_{ee}(k)\chi_e^0(k,\omega)}{1 + \varphi_{ee}(k)G_e(k)\chi_e^0(k,\omega)}, \tag{1}$$

with $\varphi_{ee}(k)/k^2$ the Fourier transform of the interparticle potential, and $\chi_e^0(k,\omega)$ the response function of the equivalent free fermion system.

It is a gratifying feature of the present formulation that relativistic stopping powers estimated in Sec. III with true LFC's pertaining to a dense electron fluid yield data differing by less than 10^{-4} from those with $G(k) \equiv 0$. So the RPA (mean field) approximation for $\varepsilon(k,\omega)$ with $G(k)=0$ proves highly adequate for the situation at hand.

This allows us to consider TEF degeneracy effects through

$$\varphi_{ee}(k)\chi_e^0(k,\omega) = F_1(k,\omega) + iF_2(k,\omega),$$

with [a_0 is the Bohr radius $(4\pi/3)r_s^3 = 1/na_0^2$]

$$F_1 = (k,\omega) = -\frac{\alpha r_s}{4\pi Q}\left[\phi\left(\frac{z}{Q}+Q\right) - \phi\left(\frac{z}{Q}-Q\right)\right] \tag{2}$$

and

$$F_2(k,\omega) = -i\frac{\alpha r_s \theta}{8Q^3}\ln\left[\frac{1+\exp\left[\eta - \frac{1}{\theta}\left(\frac{z}{Q}-Q\right)^2\right]}{1+\exp\left[\eta - \frac{1}{\theta}\left(\frac{z}{Q}+Q\right)^2\right]}\right], \tag{3}$$

where $\alpha = (4/9\pi)^{1/3}$, η is the chemical potential, $Q = k/2k_F$, $k_F = (3\pi^2 n)^{1/3}$ is the Fermi wave number, and $z = \hbar\omega/4E_F$. $\phi(x)$ has the form

$$\phi(x) = \int_0^\infty dy \frac{y}{1+\exp(y^2/\theta - \eta)}\ln\left|\frac{x-y}{x+y}\right|. \tag{4}$$

Expressions (1), (2), and (3) are valid for any temperature and in the limiting case of large temperatures ($\theta \gg 1$) they yield back the dielectric function of a classical electron plasma,

$$\varepsilon(k,\omega) = 1 + \frac{k_{De}^2}{k^2} W\left(\frac{\omega}{k v_{Te}}\right), \tag{5}$$

where $k_{De} = 1/\lambda_{De}$ is the inverse of the electron Debye length, v_{Te} is the electron thermal velocity, and (Fried-Conte) [12]

$$W(z) = 1 - z\exp\left(-\frac{z^2}{2}\right)\int_0^z dy \exp\left(\frac{y^2}{2}\right) + i\sqrt{\frac{\pi}{2}} z \exp\left(-\frac{z^2}{2}\right). \tag{6}$$

Calculations of the longitudinal dielectric function (1) of the partially degenerate electron fluid were then performed employing methods proposed in Refs. [7–10]. The validity of the dielectric function calculation has been confirmed through adequate sum rules.

III. RELATIVISTIC ELECTRON ENERGY LOSSES IN PLASMA

It is well known that a relativistic charged particle moving in a plasma transfers its energy mostly to the surrounding electronic matter. A theoretical description of this process can be performed using the standard expression [13]

$$\begin{aligned} -\frac{dE}{dx} &= -\frac{e^2}{\pi v^2}\int_0^\infty dk\, k \int_{-kv}^{kv} d\omega\, \omega \\ &\quad \times \mathrm{Im}\frac{1 - v^2\varepsilon(k,\omega)/c^2}{\varepsilon(k,\omega)[k^2 - \omega^2\varepsilon(k,\omega)/c^2]} \\ &\equiv -\frac{e^2}{\pi v^2}\int_0^\infty dk\, F(k), \end{aligned} \tag{7}$$

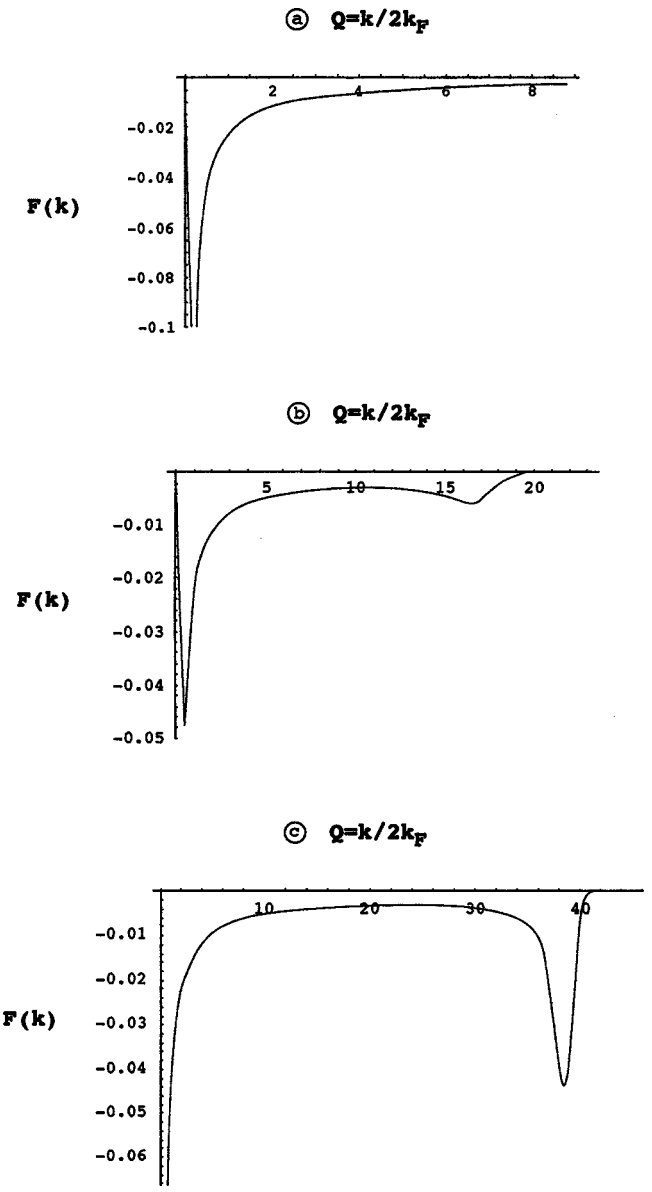

FIG. 2. Plot of $F(k)$ [Eq. (8)] at $T=T_F$ ($\theta=1$) (a) with classical $\varepsilon(k,\omega)$ [Eqs. (5) and (6)] $E=2$ MeV, $n=10^{26}$ e cm^{-3}; (b) with quantum $\varepsilon(k,\omega)$ [Eqs. (2) and (3)], $E=2$ MeV, $n=10^{26}$ e cm^{-3}; (c) with quantum $\varepsilon(k,\omega)$, $E=20$ MeV, $n=10^{25}$ e cm^{-3}.

where e and v are the charge and velocity of the projectile (electron), and c is the speed of light. The dielectric function expressions (1)–(3) used in this work give as accurate quantum-mechanical space and time dispersion description of the electromagnetic field in the plasma medium. Consequently, evaluation of the expression (7) with the dielectric functions (1)–(3) provides the full (polarizational + collisional) charged particle energy losses in contrast to the case of calculation of (7) with the classical (5) or dispersionless dielectric functions used earlier.

This intriguing feature arises from the quantum formulation (2) and (3) for $\varepsilon(k,\omega)$. It is vividly documented on Fig. 2 with plots of the k integrand in Eq. (7), i.e.,

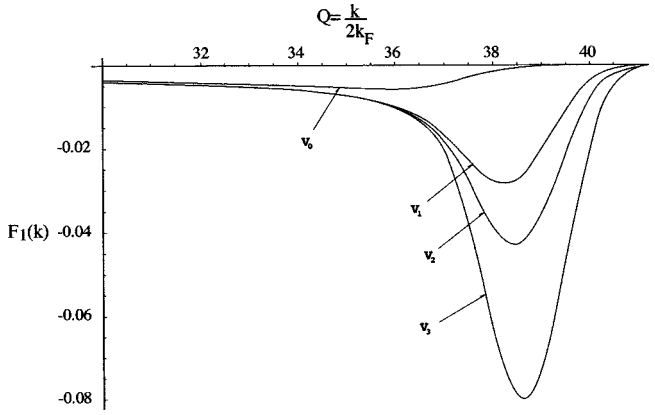

FIG. 3. Plot of $F_1(k)$ [Eq. (8′)], $n=10^{25}$ e cm^{-3}, $T=T_F$ in terms of projectile velocity v and energy E: (a) $v_0/c=0.9706$, $E_0=1$ MeV; (b) $v_1/c=0.9987$, $E_1=5$ MeV; (c) $v_2/c=0.9997$, $E_2=10$ MeV; (d) $v_3/c=0.9999$, $E_3=50$ MeV.

$$F(k) = -k\int_{-kv}^{kv} d\omega\,\omega\,\mathrm{Im}\frac{1-v^2\varepsilon(k,\omega)/c^2}{\varepsilon(k,\omega)[k^2-\omega^2\varepsilon(k,\omega)/c^2]}, \quad (8)$$

given for the Fried-Conte classical expressions (5) and (6) [see Fig. 2(a)] and the quantum RPA ones (2) and (3) in terms of $Q=k/2k_F$, for $n=10^{26}$ e cm^{-3} and electron energy $E=2$ MeV [Figs. 2(a) and 2(b)] and 20 MeV [Fig. 2(c)] at $n=10^{25}$ e cm^{-3}. The quantum profiles are seen to display left and right conspicuous peaks respectively located at $k=2k_F$ and $\cong 2.246mv^2/e^2$. They correspond to collective long-range and collision short-range contributions, respectively. The classical profile [Fig. 2(a)] shows only the long-range peak. The collision peak increases in magnitude with E. In this connection, it is instructive to zoom the large k section of Figs. 2(b) and 2(c) and replace Eq. (8) with half of it,

$$F_1(k) = -k\int_{0}^{kv} d\omega\,\omega\,\mathrm{Im}\frac{1-(v^2/c^2)\varepsilon(k,\omega)}{\varepsilon(k,\omega)[k^2-(\omega^2/c^2)\varepsilon(k,\omega)]}. \quad (8')$$

Expression (8′) is thus plotted on Fig. 3 for $n=10^{25}$ e cm^{-3}, $\theta=1$ with $1\leqslant E\leqslant 50$ MeV. It obviously documents the energy collisionally transferred from the electron projectile to the target electron, with maximum value $mc^2(\gamma-1)$ in terms of the Lorentz parameter γ.

At this point we think it of interest to contrast (see Fig. 4) the present quantum evaluations of REB energy losses with earlier estimates based on a combination of collective stopping arising from the excitation of Langmuir collective modes [14]

$$-\frac{dE}{dx} = \frac{2\pi ne^4}{m\beta^2c^2}\ln\left[\frac{v}{\omega_p\lambda_D}\left(\frac{2}{3}\right)^{1/2}\right]^2, \quad (9)$$

in terms of the target electron plasma frequency ω_p, with a plasma adapted Möller relativistic expression for collisional energy losses given by [15]

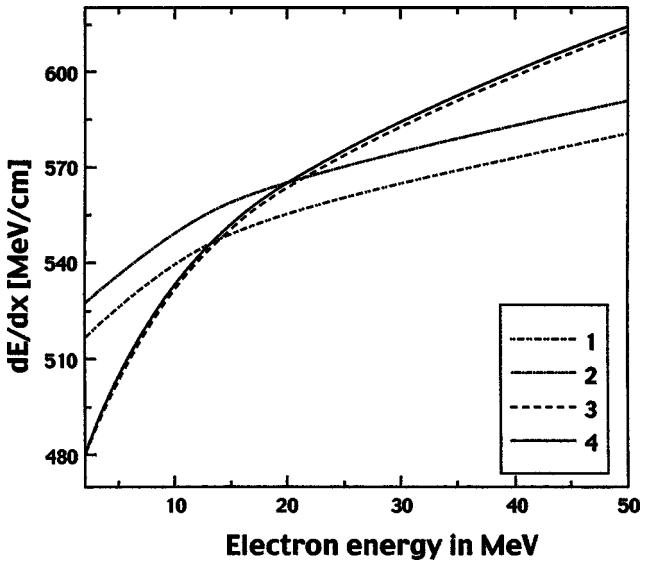

FIG. 4. Stopping power in plasma with $n=10^{26}$ cm^{-3}. (Curve 1) Classical polarization [Eq. (9)]+ collisional energy losses in plasma [Eq. (10)], with $\theta=1$. (Curve 2) Classical polarization [Eq. (9)] + collisional energy losses in plasma [Eq. (10)], with $\theta=2$. (Curve 3) Our numerical calculation with quantum dielectric function [Eqs. (2) and (3)] in plasma with $\theta=1$. (Curve 4) Our numerical calculation with quantum dielectric function [Eq. (2) and (3)] in plasma with $\theta=2$.

$$-\frac{dE}{dx}=\frac{2\pi ne^4}{m\beta^2c^2}\left\{\ln\frac{1}{2\tau_{\min}}+0.125\left(\frac{\tau}{\tau+1}\right)^2-\frac{(2\tau+1)}{(\tau+1)^2}\ln 2+1-\ln 2\right\}, \tag{10}$$

where $\tau_{\min}^{1/2}$ is the ratio of the de Broglie wave length λ_e of the relativistic projectile electrons to the target Debye length,

$$\tau_{\min}^{1/2}=\frac{\lambda_e}{\lambda_D}=\frac{(\hbar/mv)\sqrt{1-\beta^2}}{\lambda_D}, \quad \tau=\gamma-1$$

with

$$\gamma=(1-\beta^2)^{-1/2} \text{ and } \beta=v/c.$$

A quick glance at Fig. 4 confirms that despite significant quantitative discrepancies, the quantum and classical stopping share the same basic trends.

IV. GLOBAL FEATURES

A first and highly conspicuous overall feature displayed by quantum stopping estimates is a very small temperature dependence for $0.2\leqslant\theta\leqslant 5$. This is true at moderate REB energy ($E=1$ MeV on Fig. 5) and at high energy ($E=50$ MeV, Fig. 6) as well, as long as $n\leqslant 10^{26}$ e cm^{-3}. At higher target densities, the θ splitting of the various stopping profiles becomes increasingly more noticeable. Such a behavior confirms similar trends shared by classical target calculations with a temperature above 1 keV.

Increasing E in the ultrarelativistic domain causes to appear a striking difference between quantum (curve 1 on Fig. 7) and classical (curve 2 on Fig. 7) stopping calculations. On Fig. 7, the curve 3 depicts a convenient asymptotic formula featuring polarization energy losses of the ultrarelativistic electron [13] ($v=c$),

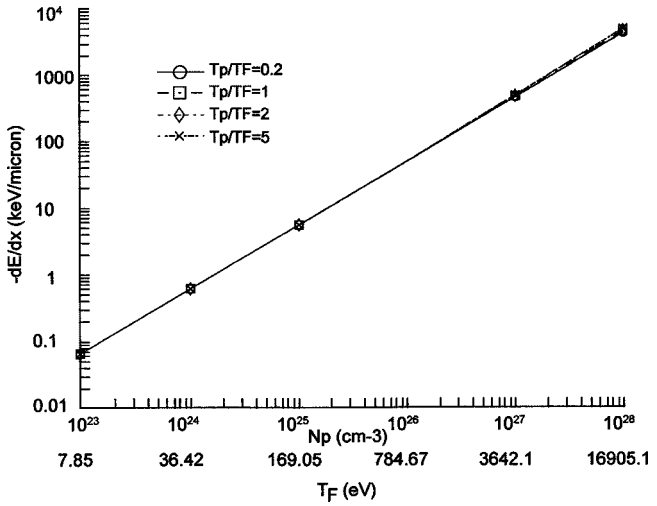

FIG. 5. REB stopping at 1 MeV in TEF in terms of electron number density n and Fermi temperature T_F.

$$-\frac{dE}{dx}=\frac{2\pi ne^4}{mc^2}\ln\left(\frac{mc^2k_{\max}^2}{4\pi nc^2}\right), \tag{11}$$

with $k_{\max}$ the inverse of the closest approach distance.

Classical stopping (curve 2) is seen to decay with increasing E at high velocity, in agreement with standard and nonrelativistic Bethe-like behavior $\sim v^{-2}$. On the other hand, quantum stopping (curve 1) exhibits a steadily monotonic increase with E, in the same relativistic velocity range. This *a priori* counterintuitive behavior is actually in agreement with an argument already presented in Jackson's textbook [16] when $v\sim c$; the Bethe-like prefactor gets saturated at c^{-2} while the factoring stopping number can still increase with E. What is actually surprising in the present context, is that we need a full fledged TEF quantum qualification to docu-

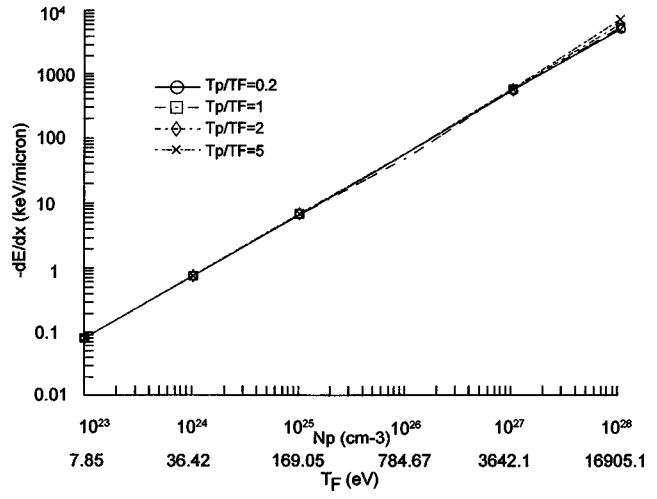

FIG. 6. Same as in Fig. 5 for 50 MeV REB.

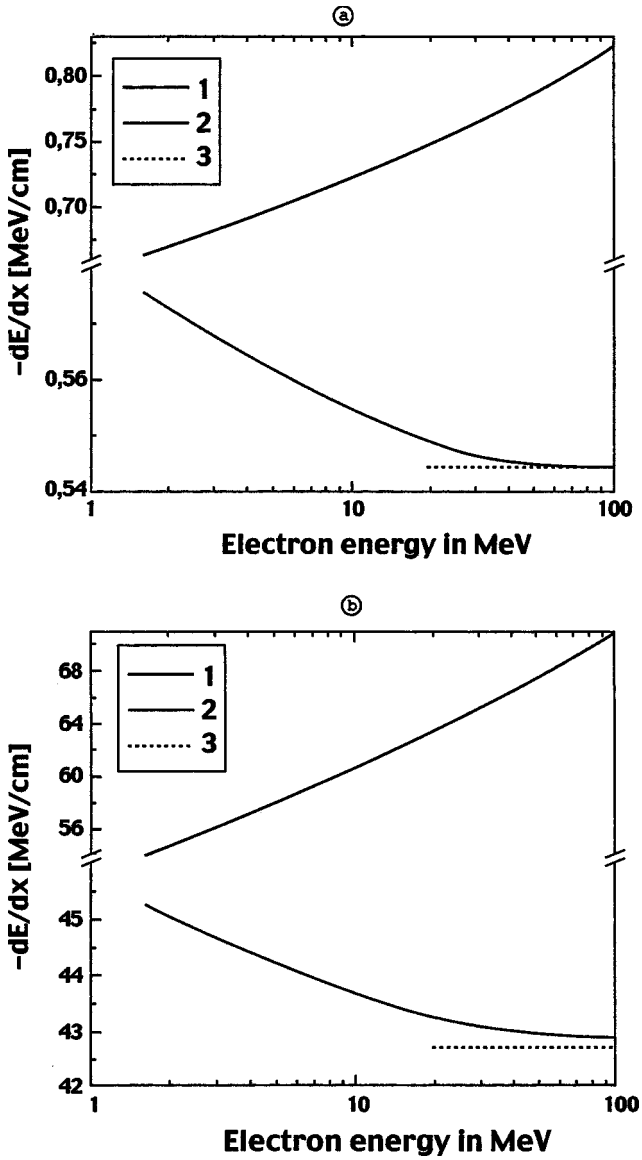

FIG. 7. REB stopping in target electron fluid at $\theta=5$ in terms of electron projectile energy. Curve 1, quantum $\varepsilon(k,\omega)$ [Eqs. (2) and (3)]; curve 2, classical $\varepsilon(k,\omega)$ [Eqs. (5) and (6)]; curve 3, asymptotic expression (11). $n=$(a)10^{23} and (b)10^{25} e cm^{-3}.

ment a straightforward and relativistic kinematic trend.

The following expression has been obtained as a careful pseudoanalytic fit to quantum stopping results. It is essentially accurate for $n \leqslant 10^{26}$ e cm^{-3}, as evidenced from stopping data contrasted in Table I. It reads as

$$-\frac{dE}{dx}=\frac{4\pi ne^4}{mv^2}\ln\left(\frac{2mc^2\gamma^2}{\hbar\omega_p}\right). \qquad (11')$$

TABLE I. Approximate [Eq. (11′)] vs quantum stopping powers (in MeV/cm).

Projectile velocity and energy		Approximation formula (11′)	Quantum data			
β	E (MeV)		$\theta=0.2$	%	$\theta=5$	%
			$n=10^{23}$ cm^{-3}			
0.94108	1	0.6774	0.6848	1.1	0.6848	1.1
0.97908	2	0.6529	0.6620	1.4	0.6620	1.4
0.99569	5	0.6717	0.6814	1.4	0.6814	1.4
0.99882	10	0.7005	0.7103	1.4	0.7103	1.4
0.99969	20	0.7334	0.7432	1.3	0.7432	1.3
0.99995	50	0.7789	0.7888	1.3	0.7888	1.3
			$n=10^{24}$ cm^{-3}			
0.94108	1	6.1109	6.1850	1.2	6.1873	1.2
0.97908	2	5.9160	6.0072	1.5	6.0099	1.6
0.99569	5	6.1245	6.2215	1.6	6.2246	1.6
0.99882	10	6.4163	6.5143	1.5	6.5177	1.6
0.99969	20	6.7462	6.8445	1.4	6.8483	1.5
0.99995	50	7.2023	7.3007	1.4	7.3049	1.4
			$n=10^{25}$ cm^{-3}			
0.94108	1	55.481	55.227	1.4	55.331	1.5
0.97908	2	53.036	53.955	1.7	54.074	1.9
0.99569	5	55.324	56.302	1.7	56.441	2.0
0.99882	10	58.278	59.268	1.7	59.422	1.9
0.99969	20	61.588	62.582	1.6	62.751	1.9
0.99995	50	66.152	67.148	1.5	67.339	1.8
			$n=10^{26}$ cm^{-3}			
			$\theta=0.2$	%	$\theta=5$	%
0.94108	1	478.52	486.24	1.6	490.60	2.5
0.97908	2	469.12	478.61	2.0	483.72	3.0
0.99569	5	494.02	504.19	2.0	510.25	3.2
0.99882	10	523.94	534.27	1.9	541.07	3.2
0.99969	20	557.14	567.56	1.8	575.12	3.1
0.99995	50	602.81	613.31	1.7	621.88	3.1
			$n=10^{28}$ cm^{-3}			
0.94108	1	34595	35971	3.8	38338	9.8
0.97908	2	34664	36374	4.7	44995	22.9
0.99569	5	37560	39535	5.0	55346	32.1
0.99882	10	40625	42761	5.0	62941	35.5
0.99969	20	43965	46223	4.9	69589	36.8
0.99995	50	48538	50731	4.3	76400	36.5

V. RANGE AND PENETRATION DEPTH

Up to now, REB penetration in dense and supercompressed DT plasma has been essentially viewed as a two-step process. First, projectile electrons lose their kinetic energy through inelastic collisions with the TEF considered classically. Then, the projectile trajectories get deflected by elastic and multiple scattering on the TIF.

This latter mechanism advocates for nonrectilinear REB trajectories in cold matter as well as in hot plasmas. As a consequence, the overall projectile particle range R in the target is presumably much larger than the effective penetration depth, measured (for instance) from a given tangential plane to a precompressed target. These arguments have already led us in the classical case to use the relationship [17]

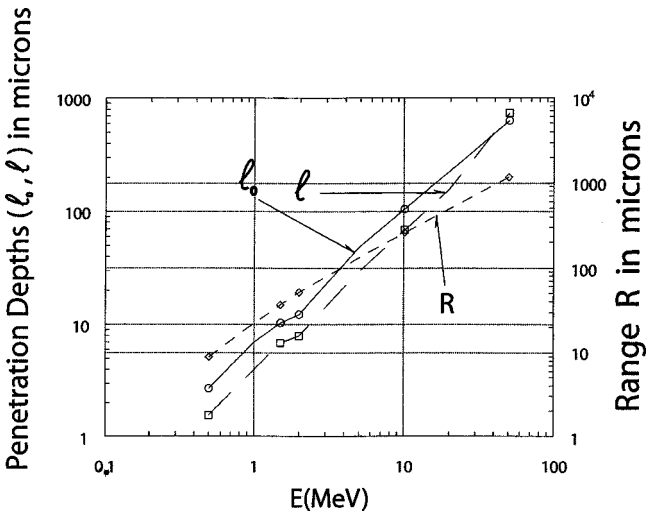

FIG. 8. Range and penetration depths ℓ and ℓ_0 in a DT target with 300 g/cm^3 density and $T=T_F$. ℓ_0 denotes the penetration depth restricted to the quadratic term in the right-hand side of Eq. (12).

$$R = \ell + \frac{\ell^2}{2\bar{\lambda}} + \frac{\ell^3}{2\bar{\lambda}^2}, \tag{12}$$

connecting range R and effective penetration depth ℓ. Equation (12) indeed includes any projectile orientation out of a fixed framing plane, mimicking, for instance, a virtual photographic plate. In Eq. (12), $\bar{\lambda}$ features the β average [6]

$$\frac{1}{\bar{\lambda}} = (\beta_{\max} - \beta_{\min})^{-1} \int_{\beta_{\min}}^{\beta_{\max}} \frac{d\beta}{\lambda} \tag{13}$$

for the square average deflection per unit path length [18] ($Z=1$, $A=2.5$)

$$\lambda^{-1}\ (\mathrm{cm}^{-1}) = 8\pi \left(\frac{e^2}{m_e c^2}\right)^2 \frac{Z(Z+1)}{A\beta^4}(1-\beta^2) N_A \rho \times \left[\ln\left(\frac{137\beta}{Z^{1/3}(1-\beta^2)^{1/2}}\right) + \ln(1.76) - \left(1+\frac{\beta^2}{4}\right)\right] \tag{14}$$

in terms of the Avogadro number N_A and target density in g/cm^3. Z and A denote the usual electric and atomic numbers for the target nuclei. Here $Z=1$ and $A=2.5$ for an equiatomic DT mixture.

On Fig. 8, the REB range R is contrasted with the penetration depths ℓ and ℓ_0. The latter quantity refers to Eq. (12) with the cubic term deleted in its right-hand side. ℓ_0 corresponds to multiple scattering restricted to small angle deflections. On the other hand, the cubic term secures contributions from rare but large angle scattering events.

It should be appreciated that the present R quantum estimates are nearly a factor of 2 er than classical ones based on Eqs. (9) and (10) obtained in the same beam-target conditions.

A relevant and somewhat detailed tabulation of quantum R values (in micrometers) is provided in Table II for a DT target at 300 g/cm^3 and various temperatures.

TABLE II. Quantum REB ranges in micrometers computed between $E(\beta_1)$, the initial energy, and $E(\beta_0)=E(\beta_1)/20$ for a DT target at 300 g/cm^3 and several θ values.

Projectile initial energy (MeV)	Velocities ($\beta=v/c$) $\beta_0-\beta_1$	Relativistic ranges $\theta=0.2$	$\theta=1$	$\theta=5$
0.5	0.3018–0.8629	9.01	9.00	8.99
1	0.4127–0.9411	22.68	22.67	22.58
1.5	0.4895–0.9672	37.03	37.00	36.82
2	0.5482–0.9791	51.41	51.37	51.09
5	0.7410–0.9957	134.55	134.43	133.52
10	0.8629–0.9988	263.61	263.31	261.37
20	0.9411–0.9997	504.21	503.58	499.59
50	0.9855–0.9999	1171.74	1170.32	1160.23

The three pertinent lengths R, ℓ, and ℓ_0 satisfy the obvious inequalities

$$\ell < \ell_0 < R, \tag{15}$$

as confirmed on Fig. 8.

VI. OUTLOOK: RELEVANCE TO FAST IGNITION

We focused attention on stopping mechanisms affecting REB's considered in the MeV energy range, and interacting with an arbitrary degenerate electron fluid at densities $n \geqslant 10^{23}\ e\ \mathrm{cm}^{-3}$. In particular, we intended to stress specific stopping features due to the target electron degeneracy. This is efficiently performed within a RPA framework which allows us to include in a single formulation long-range effects as well as those of short-range collisions on the projectile energy loss. Then we confirmed a very small θ dependence of the relativistic stopping results, already evidenced in previous classical ($\theta \gg 1$) TEF modeling. We also checked that the expected increase of stopping power with relativistic kinetic energy demands that the TEF degeneracy be taken into account. Finally, an efficient compact and pseudoanalytic expression [Eq. (11′)] has been obtained in the ultrarelativistic limit.

As far as the feasibility of the FI concept is considered we got a factor of 2 reduction for the REB penetration depth in the core of precompressed DT fuel.

So ignition scenarios based on the former classical TEF formulation remain basically unchanged [19], as well as their provisional expectations.

As a final point it has to be recalled that the most deleterious effect that could prevent an efficient REB penetration toward the dense fuel core is featured by the Weibel electromagnetic instability (WEI), able to divert swiftly and transversally to the initial REB orientation a significant fraction of its kinetic energy. So, a crucial figure of merit is the number of WEI e-foldings

$$N_{e\text{-fold}} = \delta_{\max} T_{\mathrm{stop}}, \tag{16}$$

in terms of the REB relativistic stopping time

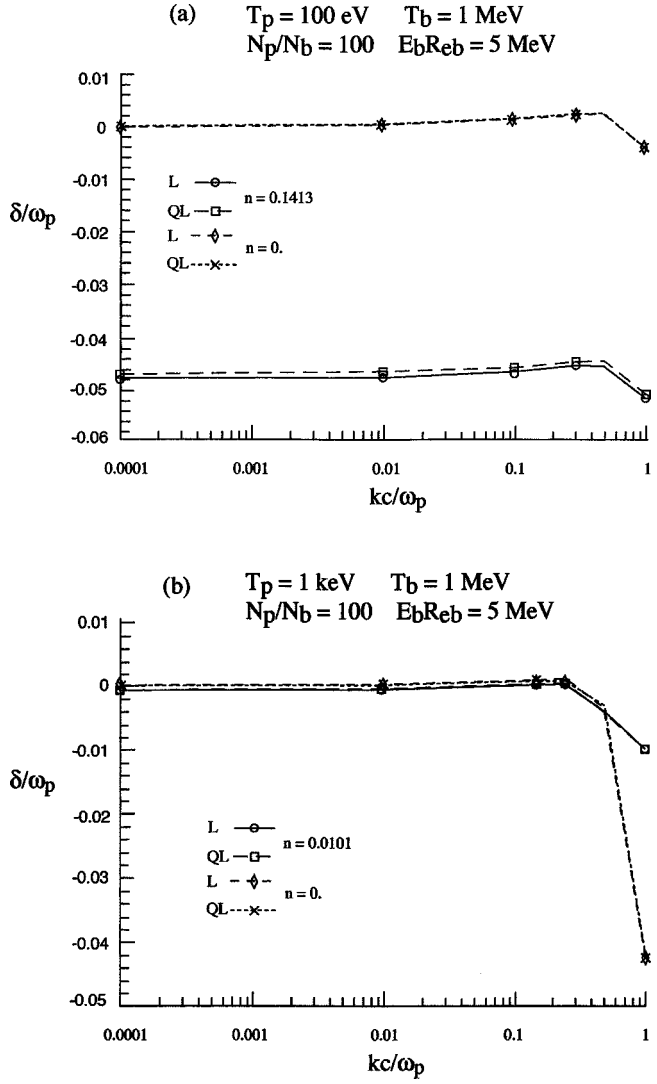

FIG. 9. Linear and quasilinear electromagnetic growth rates for a 5 MeV REB with $n_b = 10^{22} e\ \mathrm{cm}^{-3}$ and $T_b = 1$ MeV impinging an electron target with $n_p = 100 n_b$ and $T_p = 100$ (a) and 1 keV (b). Curves are parametrized with respect to to normalized collision frequencies n(target) with negligible intrabeam scattering ($n_1 = 0$).

$$T_{\mathrm{stop}} = \frac{1}{c}\int_{E_b^{\min}}^{E_b^{\max}} \frac{1+\dfrac{E_b}{m_e c^2}}{\left[\left(\dfrac{E_b}{m_e c^2}\right)\left(\dfrac{E_b}{m_e c^2}+2\right)\right]^{1/2}} \frac{dE_b}{dE_b/dx}$$

$$\cong \frac{100}{4} \times (10^{-4}\ \mathrm{cm}) \times \frac{1}{\beta_{bc}(\mathrm{cm/s})}$$

$$\cong 10^{-13}\ \mathrm{s\ for\ a\ 1\ MeV\ REB} \tag{17}$$

traveling through 25 μm of a constant density TEF.

We left to a forthcoming work the investigation of in-flight electron-electron correlations in a dense REB impinging on a quantum TEF. Previous studies restricted to a classical target already documented a substantial range shortening arising from these relativistic and dynamical two-body intrabeam correlations [20].

We now turn to estimating the $\delta_{\max}$ implied in Eq. (16).

The interaction processes involved in the stopping of intense relativistic electron beams are monitored by a competition between collisionally dominated stopping mechanisms and nearly instantaneous beam energy loss due to fast rising electromagnetic instabilities [21].

Let us now consider a current neutral beam-plasma system. The relativistic REB propagates with the velocity v_d^b and the plasma return current flows with velocity v_d^p. It is reasonable to assume that an electromagnetic mode has k normal to v_d^b, perturbed electric field **E** parallel to v_d^b, and perturbed magnetic field **B** normal to both v_d^b and **E**. So the total asymmetric f_0 consists of nonrelativistic background electrons and relativistic beam electrons [22]

$$f_0(\mathbf{p}) = \frac{n_p}{2\pi m(\theta_x^p \theta_y^p)^{1/2}} \exp\left(-\frac{(p_x + p_d^p)^2}{2m\theta_x^p} - \frac{p_y^2}{2m\theta_y^p}\right) + \frac{n_b}{2\pi m\gamma(\theta_x^b \theta_y^b)^{1/2}} \exp\left(-\frac{(p_x + p_d^b)^2}{2m\gamma\theta_x^b} - \frac{p_y^2}{2m\gamma\theta_y^b}\right). \tag{18}$$

Here θ_x and θ_y are the temperature components parallel to the x and y directions, $\mathbf{p}_d$ is the drift momentum, the superscripts p and b represent the plasma and the beam electron, respectively. From the linearized Vlasov equation with collision term ν and linearized Maxwell's equations we get linear dispersion relations for a purely growing mode. The collision term $\nu = \nu_p + \nu_b$ is explained as a superposition of target and beam plasma contributions. In Eq. (18) the drift momentum should read as

$$p_d^b = m\gamma v_b \quad \text{and} \quad p_d^p = p_d^b \frac{n_b}{\gamma n_p} \tag{19}$$

in terms of $\gamma = (1 - v_b^2/c^2)^{-1/2}$ and v_b, the beam velocity.

The WEI growth rates and wave number obviously take the forms (ω_p is the target plasma frequency)

$$x = \frac{\delta}{\omega_p} \quad \text{and} \quad y = \frac{kc}{\omega_p} \tag{20}$$

with corresponding normalized collision frequencies [23]

$$n_1 = \frac{\nu_b}{\omega_p} \quad \text{and} \quad n = \frac{\nu_p}{\omega_p}. \tag{21}$$

Transverse velocities play a pivotal role in the WEI growth rate analysis. They read, respectively, as

$$v_1 = \frac{v_y^b}{c} \quad \text{and} \quad v_2 = \frac{v_y^p}{c} \tag{22}$$

together with the beam-target density ratio

$$r = \frac{n_b}{\gamma n_p}. \tag{23}$$

With these expressions, one can then specialize the evaluation of the plasma Fried-Conte dielectric function through suitable asymptotic expansions. This procedure then leads to four typical beam-target combinations based on the asymmetry parameters,

$$A = \frac{\theta_x^p + p_d^{p2}/m}{\theta_y^p}, \quad B = \frac{\theta_x^b + p_d^{b2}/m\gamma}{\theta_y^b}. \tag{24}$$

Up to now we restricted our attention to a linear WEI analysis. More accurate growth rates (GR) are expected by retaining particle motion in the target plasma under local electric and magnetic fields. Sophisticated treatments refer to the Dupree-Weinstock analysis [24] of the so-called weak turbulence. In the present context these considerations lead us to complete specification of A and B with [23]

$$A' = \frac{AT_p}{T_p + XD}, \quad B' = \frac{BT_b}{T_b + XD}, \tag{25}$$

where X denotes the largest solution of

$$(1+r)X^4 - \left[r\frac{p_d^{b2}}{(m\gamma)^2} + \frac{\theta_x^p}{m} + \frac{p_d^{p2}}{m^2} - (1+r)\left(\frac{\theta_y^p}{m} + \frac{\theta_y^b}{m}\right)\right]X^2 - \left[r\frac{p_d^{b2}}{(m\gamma)^2}\frac{\theta_y^p}{m}\left(\frac{\theta_x^p}{m} + \frac{p_d^{p2}}{m^2}\right)\frac{\theta_y^b}{m\gamma} - (1+r)\frac{\theta_y^p}{m}\frac{\theta_y^b}{m\gamma}\right] = 0, \tag{26}$$

and $D = 511r(1-\gamma^{-2})$. T_p and T_b are in keV. In the following we shall restrict attention to isotropic distributions with $\theta_x^p = \theta_y^p$ and $\theta_x^b = \theta_y^b$.

Typical REB target interactions of FI interest are depicted on Figs. 9(a) and 9(b) through linear (L) and quasilinear (QL) growth rates.

Increasing significantly the target plasma density and the beam temperature (Fig. 9) make negligible the intrabeam collision term satisfying now $n_1 << n$. The very high T_b value, in the MeV range, erases very efficiently any positive growth rate, thus featuring a beam-target interaction stable at any plasma wave number k.

These preliminary results highlight the cone-angle scenario [25,2] with laser produced electrons close to the highest density core in precompressed DT fuel. In this case, with $\delta_{\max} \leqslant 0$, one obviously keeps $N_{e\text{-fold}} = 0$. In practice, $N_{e\text{-fold}} \leqslant 5-6$ appears tolerable which means $\delta_{\max} < 10^{14}\ \mathrm{s}^{-1}$ [cf. Eq. (17)].

ACKNOWLEDGMENTS

We are deeply indepted to Professor J. J. Honrubia from UPM (Madrid) for suggesting the present work. K.V.S. is also deeply grateful to the NATO authorities in Paris for a grant allowing him to pursue the present endeavor at Orsay.

[1] M. Tabak, J. Hammer, M. E. Glinsky, W. L. Kruer, S. C. Wilks, J. Woodworth, E. M. Campbell, M. D. Perry, and R. J. Mason, Phys. Plasmas **1**, 1626 (1994).
[2] C. Deutsch, Eur. Phys. J.: Appl. Phys. **24**, 95 (2003).
[3] J. J. Honrubia (private communication).
[4] J. Lindl, Phys. Plasmas **2**, 3933 (1995).
[5] D. Umstadter, J. Phys. D **36**, R151 (2003).
[6] C. Deutsch, H. Furukawa, K. Mima, M. Murakami, and K. Nishihara, Phys. Rev. Lett. **77**, 2483 (1996).
[7] S. Skupsky, Phys. Rev. A **16**, 727 (1977).
[8] C. Gouedard and C. Deutsch, J. Math. Phys. **19**, 32 (1978); C. Deutsch and G. Maynard, Recent Res. Devl. Plasmas **1**, 1 (2000).
[9] N. R. Arista and W. Brandt, Phys. Rev. A **29**, 1471 (1984).
[10] R. G. Dandrea, N. W. Ashcroft, and A. E. Carlsson, Phys. Rev. B **34**, 2097 (1986).
[11] K. Utsumi and S. Ichimaru, Phys. Rev. A **26**, 603 (1982); Phys. Rev. B **23**, 13 291 (1981).
[12] B. D. Fried and S. D. Conte, *The Plasma Dispersion Function* (Academic Press, New York, 1961), p. 1.
[13] L. D. Landau and E. M. Lifschitz, *Electrodynamics of Continuous Media* (Nauka, Moscow, 1982), p. 623 (in Russian).
[14] D. Bohm and D. Pines, Phys. Rev. **85**, 338 (1952).
[15] V. V. Val'chuk, N. B. Volkov, and A. P. Yalovets, Plasma Phys. Rep. **21**, 159 (1995).
[16] J. D. Jackson *Classical Electrodynamics*, 2nd ed. (Wiley, Sons, New York, 1975), p. 629.
[17] P. C. Hemmer and I. E. Farquahr, Phys. Rev. **168**, 294 (1968).
[18] H. H. Hubbel and R. D. Birkoff, Phys. Rev. A **26**, 2460 (1982).
[19] S. Atzeni, Phys. Plasmas **6**, 3316 (1999); A. R. Piriz and M. M. Sanchez, *ibid.* **5**, 4373 (1998), which predicts ignition with 10 times less energy than does Atzeni.
[20] C. Deutsch and P. Fromy, Phys. Plasmas **6**, 3597 (1999); Phys. Rev. E **61**, 4322 (2000).
[21] A. Bret, M. C. Firpo, and C. Deutsch, Phys. Rev. E **70**, 046401 (2004).
[22] T. Okada and K. Niu, J. Plasma Phys. **23**, 423 (1980).
[23] C. Deutsch, Laser Part. Beams **22**, 115 (2004).
[24] M. Kono and Y. H. Ichikawa, Prog. Theor. Phys. **49**, 754 (1973).
[25] R. Kodama *et al.*, Nature (London) **412**, 798 (2001).